NUMERICAL INVESTIGATION OF AN INTERNAL LAYER IN TURBULENT FLOW OVER A CURVED HILL

S.-W. Kim*
Institute for Computational Mechanics in Propulsion
NASA Lewis Research Center
Cleveland, Ohio

ABSTRACT

Numerical investigation of incompressible and compressible turbulent flows over strongly curved surfaces is presented. The turbulent flow equations are solved by a pressure based Navier-Stokes equations solver. In the method, the conservation of mass equation is replaced by a pressure correction equation applicable for both incompressible and compressible flows. The turbulence is described by a multiple-time-scale turbulence model supplemented with a near-wall turbulence model. The numerical results show that the internal layer is a strong turbulence field which is developed beneath the external boundary layer and is located very close to the wall. The development of the internal layer is attributed to the enormous mean flow strain rate caused by the streamline curvature. The external boundary layer flow responds rather slowly to the streamline curvature, thus the turbulence field in the forward corner of the curved hill is characterized by two turbulence fields (one belongs to the external boundary layer flow and the other belongs to the internal) interacting with each other. The turbulence intensity of the internal layer is much stronger than that of the external boundary layer so that the development of a new boundary layer in the downstream region of the curved hill depends mostly on the internal layer. These numerical results are in good agreement with the measured data, and show that the turbulence model can resolve the turbulence field subjected to the strong streamline curvature.

NOMENCLATURE

A_u	coefficient for u-velocity correction equation
A_v	coefficient for v-velocity correction equation
c	chord length of axisymmetric bump
c_f	friction coefficient
c_p	pressure coefficient
$c_{p\ell}$	turbulence model constants for ϵ_p equation ($\ell=1,3$)
$c_{t\ell}$	turbulence model constants for ϵ_t equation ($\ell=1,3$)
$c_{\mu f}$	constant coefficient (=0.09)
f_μ	wall damping function for eddy viscosity equation
f_ϵ	wall damping function for ϵ_w equation
k	turbulent kinetic energy ($k=k_p + k_t$)
k_p	turbulent kinetic energy of eddies in production range
k_t	turbulent kinetic energy of eddies in dissipation range
k_e	effective thermal conductivity ($=k_m + C_p\mu_t/\sigma_T$)
k_m	molecular thermal conductivity
M_∞	free stream Mach number
U_∞	free stream velocity
p	static pressure
P_r	production rate of turbulent kinetic energy

R	gas constant
R_e	Reynolds number
R_t	turbulent Reynolds number $(=k^2/(\nu\epsilon_1))$
s'	distance measured along the curved hill
T	temperature
(u,v)	time averaged velocities in (x,y) coordinates
$\overline{u'v'}$	Reynolds stress
V	velocity vector $(=\{u,v\})$
(x,y)	tangential and transverse coordinates
ϵ_p	energy transfer rate of turbulent kinetic energy
ϵ_t	dissipation rate of turbulent kinetic energy
ϵ_1	dissipation rate of turbulent kinetic energy
κ	von Karman constant $(=0.41)$
μ	molecular viscosity
μ_e	effective viscosity $(=\mu+\mu_t)$
μ_t	turbulent viscosity
ν	kinematic viscosity of fluid
ν_t	turbulent eddy viscosity
ρ	density
σ_{kp}	turbulent Prandtl number for k_p equation
σ_{kt}	turbulent Prandtl number for k_t equations
σ_T	turbulent Prandtl number for energy equation $(=0.75)$
$\sigma_{\epsilon p}$	turbulent Prandtl number for ϵ_p equation
$\sigma_{\epsilon t}$	turbulent Prandtl number for ϵ_t equation
τ_w	wall shearing stress
Φ	dissipation function for energy equation

Superscripts

*	current value
'	incremental (or corrective) value

INTRODUCTION

Turbulent flows subjected to various strain rates (in addition to the simple shearing strain rates) caused by streamline curvature, strong pressure gradient, separation and reattachment, swirl velocity and interaction of a multiple number of shear layers are usually called "complex turbulent flows." Calculations of complex turbulent flows using various turbulence models such as the k-ϵ turbulence models, algebraic Reynolds stress turbulence models (ARSM), and Reynolds stress turbulence models (RSM) yield rather unsatisfactory computational results (ref. 1). Many turbulence models, improved by modifying the standard form turbulence equations (usually, the dissipation rate equation for k-ϵ and ARSM and the pressure-strain correlation term for ARSM and RSM) to yield better computational results for a few flow cases, have produced worse agreement with the measured data than the standard turbulence models for other classes of turbulent flows (ref. 2). Unlike many other turbulence models, the present multiple-time-scale turbulence model (hereafter, abbreviated as the M-S model) yields accurate computational results for a number of complex turbulent flows (ref. 3-4). These complex turbulent flows include: a wall-jet, a wake-boundary layer interaction flow, a turbulent flow over a backward-facing step, a confined coaxial swirling jet, and reattaching shear layers in a divergent channel. The numerical results for each of these complex turbulent flows obtained using the M-S model compared as favorably with the measured data as the results obtained using an optimized turbulence model for each flow. More

394

recently, it was shown that the M-S model can resolve the turbulence field subjected to a strong streamline curvature in an incompressible turbulent flow over a curved hill (ref. 5) and in compressible turbulent flows over a curved hill (ref. 6). A few numerical results obtained in the previous studies are presented in this paper. A few differences between the present M-S model and that of Hanjelic et al. (ref. 7) are also reproduced here from reference 3. The historical background of experimental and theoretical researches in turbulent flows subjected to streamline curvature (ref. 5, 8-9) is briefly described below.

Turbulent shear layers over curved surfaces are highly sensitive even to a small amount of streamline curvature (ref. 8). Bradshaw (ref. 8) proposed a curvature correction method based on an assumption that such turbulent flows can be characterized by a "curvature parameter", that is, the ratio of boundary layer thickness to radius of curvature. In the curvature correction method, the mixing length is altered to include the curvature parameter. Many turbulence models incorporating a curvature correction method yield improved computational results for turbulent flows over mildly curved surfaces, and the computational results help to better understand the turbulence structure of such flows; however, these turbulence models still fail to predict the turbulence field for turbulent flows with large streamline curvature. To better understand the turbulence structure over strongly curved surfaces, Baskaran, Smits & Joubert measured various turbulence quantities in a turbulent boundary layer over a curved hill (ref. 9). The measured data showed that an internal layer is formed beneath the external boundary layer and that the internal layer is insensitive to the external boundary layer and the curvature parameter. A numerical investigation of the same turbulent flow using the M-S turbulence model showed that the internal layer is developed beneath the external boundary layer and in the region very close to the wall. It was also found that the internal layer is significantly different from boundary layer flows in the sense that the internal layer is characterized by a strong turbulence field.

The compressible turbulent flows over an axisymmetric curved hill (ref. 10) and the incompressible turbulent flow over a two-dimensional curved hill (ref. 9) share the same physical phenomenon that the turbulence fields are subjected to strong streamline curvatures. However, the compressible flow case involves extra strains caused by the shock wave - turbulent boundary layer interaction in addition to that caused by the streamline curvature. In the compressible flow case, a supersonic pocket is formed in the top region of the curved hill as the free-stream Mach number is increased. As the strength of the shock wave is increased with increasing free stream Mach number, the size of the reversed flow region grows extensively due to the shock wave - boundary layer interaction. A number of turbulence models, ranging from algebraic turbulence models to two-equation turbulence models incorporating a streamline curvature correction method, have been tested in references 11-13. It can be found in these references that various turbulence models, except the King-Johnson algebraic turbulence model (ref. 11), fail to predict the reversed flow region at low free stream Mach numbers, which indicates that these turbulence models can not resolve the turbulence field subjected to the streamline curvature. On the other hand, the numerical results obtained using the M-S turbulence model showed that there exists a reversed flow region at low free stream Mach numbers and that the size of the reversed flow region grows extensively due to the shock wave - boundary layer interaction as the free stream Mach number is increased. These numerical results indicate that the M-S turbulence model can resolve the turbulence field subjected to extra strains caused by the streamline curvature and the shock wave - boundary layer interaction (ref. 6).

REYNOLDS AVERAGED NAVIER-STOKES EQUATIONS AND NUMERICAL METHOD

The compressible turbulent flow equations are given as

$$\frac{\partial}{\partial x}(\rho u) + \frac{1}{y^j}\frac{\partial}{\partial y}(y^j \rho v) = 0. \tag{1}$$

$$\frac{\partial}{\partial x}(\rho uu) + \frac{1}{y^j}\frac{\partial}{\partial y}(y^j \rho vu) = \frac{\partial}{\partial x}(\tau_{xx}) + \frac{1}{y^j}\frac{\partial}{\partial y}(y^j \tau_{xy}) - \frac{\partial p}{\partial x} \tag{2}$$

$$\frac{\partial}{\partial x}(\rho uv) + \frac{1}{y^j}\frac{\partial}{\partial y}(y^j \rho vv) = \frac{\partial}{\partial x}(\tau_{yx}) + \frac{1}{y^j}\frac{\partial}{\partial y}(y^j \tau_{yy}) - \frac{\partial p}{\partial y} - j\frac{\tau_{\theta\theta}}{y} \tag{3}$$

$$\frac{\partial}{\partial x}(\rho C_p uT) + \frac{1}{y^j}\frac{\partial}{\partial y}(y^j \rho C_p vT) = \frac{\partial}{\partial x}\left(k_e\frac{\partial T}{\partial x}\right) + \frac{1}{y^j}\frac{\partial}{\partial y}\left(y^j k_e\frac{\partial T}{\partial y}\right) + u\frac{\partial p}{\partial x}$$

$$+ v\frac{\partial p}{\partial y} + \mu_e\Phi \tag{4}$$

where

$$\tau_{xx} = 2\mu_e\frac{\partial u}{\partial x} - \frac{2\mu_e}{3}(\nabla\cdot V),$$

$$\tau_{xy} = \tau_{yx} = \mu_e\left(\frac{\partial u}{\partial y} + \frac{\partial v}{\partial x}\right),$$

$$\tau_{yy} = 2\mu_e\frac{\partial v}{\partial y} - \frac{2\mu_e}{3}(\nabla\cdot V),$$

$$\tau_{\phi\phi} = 2\mu_e\frac{v}{y} - \frac{2\mu_e}{3}(\nabla\cdot V),$$

$$\Phi = \left\{ 2\left(\frac{\partial u}{\partial x}\right)^2 + 2\left(\frac{\partial v}{\partial y}\right)^2 + 2j\left(\frac{v}{y}\right)^2 + \left(\frac{\partial u}{\partial y} + \frac{\partial v}{\partial x}\right)^2 \right\} - \frac{2}{3}(\nabla\cdot V)^2,$$

396

$$\nabla \cdot \mathbf{V} = \frac{\partial u}{\partial x} + \frac{1}{y^j} \frac{\partial (y^j v)}{\partial y},$$

the density is obtained from the perfect gas law given as $p=\rho RT$, $j=0$ for two-dimensional flows, and $j=1$ for axisymmetric flows. The molecular viscosity and the thermal conductivity were obtained from Sutherland's laws (ref. 14). The specific heat was obtained from a curve-fitted 4-th order polynomial (ref. 15). In the present numerical method, the conservation of mass equation is replaced by a pressure correction equation valid for both incompressible and compressible flows, which is given as

$$\frac{\partial}{\partial x}\left[\frac{u^*}{RT}p'\right] + \frac{1}{y^j}\frac{\partial}{\partial y}\left[y^j\frac{v^*}{RT}p'\right] - \frac{\partial}{\partial x}\left[\rho^* A_u \frac{\partial p'}{\partial x}\right] - \frac{1}{y^j}\frac{\partial}{\partial y}\left[y^j \rho^* A_v \frac{\partial p'}{\partial y}\right] = -\nabla \cdot (\rho^* \mathbf{v}^*) \quad (5)$$

where the first two convective incremental pressure terms in the left hand side of eq. (5) take into account the hyperbolic nature of supersonic flows and enable the capture of shock waves. Details on the present numerical method can be found in references 6 and 16 and are not included in this paper. It would be sufficient to state here that the present numerical method yields accurate computational results even when highly skewed, unequally spaced, curved grids are used. A few differences between the present numerical method and the more general compressible flow solvers are discussed below.

Recall that the compressible flow equations are mostly solved by approximate factorization methods and flux splitting methods. The Beam-Warming method (ref. 17) and the MacCormack method (ref. 18) are representatives of the approximate factorization methods, and the Steiger-Warming method (ref. 19) is a representative of the flux-splitting methods. In this class of methods, the density is solved for as a primary variable and the pressure is obtained from the equation state. For incompressible flows, the pressure no longer depends on the density and hence this class of methods fails for incompressible flows. These methods can also be extended to solve incompressible flows by including an artificial compressibility into the governing flow equations (ref. 20). On the other hand, in the pressure correction methods, the incremental pressure is solved for as a primary variable, hence the method is valid for both incompressible and compressible flows. Another difference between the two classes of methods can be found in the way the second order diffusion term is treated. In the pressure correction methods, the diffusion term is incorporated into the stiffness matrix while, in the other class of methods, the diffusion term is incorporated into the system of equations as the load vector term. For turbulent flows with extensive recirculation zones, the pressure correction methods may be numerically more stable than the other class of methods, conceptually; however, the pressure correction methods have mostly been used for incompressible flows, and the approximate factorization methods and the flux splitting methods have mostly been used for compressible flows. Therefore, definitive advantages and disadvantages of these two classes of methods can not be discussed with confidence as yet.

TURBULENCE EQUATIONS

The M-S turbulence model supplemented with the near-wall turbulence model is described below. The turbulent kinetic energy and the energy transfer rate equations for the energy-containing large eddies are given as

$$\frac{\partial}{\partial x}(\rho u k_p) + \frac{1}{y^j}\frac{\partial}{\partial y}(y^j \rho v k_p) - \frac{\partial}{\partial x}\{(\mu + \frac{\mu_t}{\sigma_{kp}})\frac{\partial k_p}{\partial x}\} - \frac{1}{y^j}\frac{\partial}{\partial y}\{y^j(\mu + \frac{\mu_t}{\sigma_{kp}})\frac{\partial k_p}{\partial y}\} = \rho Pr - \rho\epsilon_p \quad (6)$$

$$\frac{\partial}{\partial x}(\rho u \epsilon_p) + \frac{1}{y^j}\frac{\partial}{\partial y}(y^j \rho v \epsilon_p) - \frac{\partial}{\partial x}\{(\mu + \frac{\mu_t}{\sigma_{\epsilon p}})\frac{\partial \epsilon_p}{\partial x}\} - \frac{1}{y^j}\frac{\partial}{\partial y}\{y^j(\mu + \frac{\mu_t}{\sigma_{\epsilon p}})\frac{\partial \epsilon_p}{\partial y}\}$$

$$= \rho c_{p1}\frac{Pr^2}{k_p} + \rho c_{p2}\frac{Pr\epsilon_p}{k_p} - \rho c_{p3}\frac{\epsilon_p^2}{k_p} \quad (7)$$

where $Pr = \nu_t \Phi$ is the production rate. The turbulent kinetic energy equation and the dissipation rate equations for the fine scale eddies are given as

$$\frac{\partial}{\partial x}(\rho u k_t) + \frac{1}{y^j}\frac{\partial}{\partial y}(y^j \rho v k_t) - \frac{\partial}{\partial x}\{(\mu + \frac{\mu_t}{\sigma_{kt}})\frac{\partial k_t}{\partial x}\} - \frac{1}{y^j}\frac{\partial}{\partial y}\{y^j(\mu + \frac{\mu_t}{\sigma_{kt}})\frac{\partial k_t}{\partial y}\} = \rho\epsilon_p - \rho\epsilon_t \quad (8)$$

$$\frac{\partial}{\partial x}(\rho u \epsilon_t) + \frac{1}{y^j}\frac{\partial}{\partial y}(y^j \rho v \epsilon_t) - \frac{\partial}{\partial x}\{(\mu + \frac{\mu_t}{\sigma_{\epsilon t}})\frac{\partial \epsilon_t}{\partial x}\} - \frac{1}{y^j}\frac{\partial}{\partial y}\{y^j(\mu + \frac{\mu_t}{\sigma_{\epsilon t}})\frac{\partial \epsilon_t}{\partial y}\}$$

$$= \rho c_{t1}\frac{\epsilon_p^2}{k_t} + \rho c_{t2}\frac{\epsilon_p\epsilon_t}{k_t} - \rho c_{t3}\frac{\epsilon_t^2}{k_t} \quad (9)$$

The eddy viscosity is given as

$$\mu_t = \rho c_\mu f\frac{k^2}{\epsilon_p} \quad (10)$$

Eqs. (6) and (8) imply that the turbulent kinetic energy is generated by the instability of the mean fluid motion, is transferred to the high wave number region, and is dissipated by the molecular viscosity of the fluid. This mathematical model is consistent with the physically observed evolution of the turbulent kinetic energy (ref. 21) except that the cascade process of the turbulent kinetic energy is over-simplified and is represented by the single energy transfer rate. This

over-simplification is still better justified than the single-time-scale turbulence models if one considers that only the generation and dissipation of turbulent kinetic energy are considered in the latter classes of turbulence models. In eq. (10), the turbulence length scale is related to the energy transfer rate of the energy-containing large eddies rather than the dissipation rate of the fine-scale eddies. The turbulence model constants are given as $\sigma_{kp}=0.75$, $\sigma_{kt}=0.75$, $\sigma_{\epsilon p}=1.15$, $\sigma_{\epsilon t}=1.15$, $c_{p1}=0.21$, $c_{p2}=1.24$, $c_{p3}=1.84$, $c_{t1}=0.29$, $c_{t2}=1.28$, and $c_{t3}=1.66$. The turbulent kinetic energy equations, eqs. (6) and (8), are defined for the entire flow domain while the energy transfer rate equation, the dissipation rate equation, and the eddy viscosity equation are valid for the flow domain away from the near-wall region.

The near-wall turbulence is described by a "partially low Reynolds number" near-wall turbulence model (ref.22). In this near-wall turbulence model, only the turbulent kinetic energy equations are extended to include the near-wall low turbulence region and the energy transfer rate and the dissipation rate inside the near-wall layer are obtained from algebraic equations. The energy transfer rate and the dissipation rate inside the near-wall layer are given as

$$\epsilon_p = \epsilon_t = \frac{\epsilon_1}{f_\epsilon} \tag{11}$$

where $\epsilon_1 = c_{\mu f}^{3/4} k^{3/2}/\kappa y$, $f_\epsilon = 1 - \exp(-A_\epsilon R_t)$, $R_t = k^2/\nu \epsilon_1$, and $A_\epsilon = c_{\mu f}^{3/2}/2\kappa^2$. The eddy viscosity for the near-wall layer is given as

$$\mu_t = \rho \, c_{\mu f} \, f_\mu \, k^2/\epsilon_1 \tag{12}$$

where $f_\mu = 1 - 1./\exp(A_1 \sqrt{R_t} + A_2 R_t^2)$, $A_1 = 0.025$, and $A_2 = 0.00001$. The eddy viscosity given as eq. (12) grows in proportion to the cubic power of the distance from the wall. It can be found in reference 22 that the near-wall analysis yields the same growth rate of the eddy viscosity in the region very close to the wall. For wall bounded turbulent flows, the equilibrium region extends from $y^+ \approx 30$ to $y^+ \approx 300$. Thus the partition between the near-wall region and the fully turbulent outer region can be located between y^+ greater than 30 and less than 300 approximately. The present near-wall turbulence model is valid for the entire flow domain of equilibrium boundary layer flows. Thus the computational results do not depend appreciably on the location of the partition. However, if the partition is located too far away from the wall (i.e., $y^+ > 1000$), then the numerical results in the near-wall region may become similar to those obtained using a k-equation turbulence model.

The capability of the present turbulence model to resolve various complex turbulence fields is discussed in this paragraph by comparing the M-S turbulence models with the single-time-scale turbulence models and by comparing the present turbulence model with that of Hanjelic et al. (ref. 7). Recall that the turbulent transport of mass and momentum is governed by the time scale of the energy-containing large eddies and the dissipation of the turbulent kinetic energy is governed by the time scale of the fine scale eddies (ref. 21). In M-S turbulence models, the turbulent transport of mass and momentum is described using the time scale of the large eddies and the dissipation rate is described using the time scale

of the fine-scale eddies. On the other hand, in the single-time-scale turbulence models such as the k-ϵ, ARSM, and RSM turbulence models, a single time scale is used to describe both the turbulence transport mechanism and the dissipation rate of turbulent kinetic energy. The single-time-scale turbulence models yield reasonably accurate computational results for simple turbulent flows; however, the predictive capability degenerates rapidly as turbulent flows to be solved become more complex. This nature may due to the use of the time scale of fine-scale eddies to describe the turbulent transport of mass and momentum. Due to the physically consistent nature of the M-S turbulence models, these turbulence models are expected to yield significantly improved computational results compared with the single-time-scale turbulence models. However, the first M-S turbulence model (ref. 7) did not quite come up to the expectations due to a few shortcomings in the closure model. These shortcomings and a few differences between the two M-S turbulence models are reproduced here from reference 3. Firstly, the eddy viscosity equation in reference 7 is given as

$$\mu_t = \rho \; c_{\mu f} \; \frac{k k_p}{\epsilon_p} \tag{13}$$

Eq. (13) implies that the small scale eddies contained in the dissipation range may not contribute significantly to the turbulent transport of mass and momentum. However, numerical calculations of complex turbulent flows show that the ratio of k_t/k_p can vary significantly in regions where the turbulence is in a strongly inequilibrium state. This anomaly can be cured if k_t is always negligibly small. However, in this case, the multiple-time-scale turbulence model can become a single-time-scale k-ϵ turbulence model. The eddy viscosity, given as eq. (13), is also inconsistent with the near wall mixing length theory or the standard wall functions unless k_t vanishes in the near-wall equilibrium region (ref. 3). Secondly, in the present M-S turbulence model, the variable energy transfer functions were obtained from a physical dimensional analysis. On the other hand, the other M-S turbulence model contains such a variable energy transfer function only in the energy transfer rate equation. Thirdly, in the present M-S turbulence model, the model constants were obtained by solving a five by five system of equations and by numerically optimizing one model constant (c_{p1}) to yield the best solutions for a fully developed channel flow and a plane jet exhausting into a moving stream (ref. 3). One equation for the model constants is obtained from the equilibrium condition. Two equations are obtained by transforming the multiple-time-scale turbulence equations into asymptotic turbulence growth rate equations which are equivalent to that of Harris, Graham & Corrsin (ref. 23). The other two equations are obtained by transforming the present turbulence equations into asymptotic turbulence decay rate equations which are equivalent to that of Harlow and Nakayama (ref. 24). Lastly, of practical importance, arbitrary ratios of k_t/k_p were used as a near wall boundary condition together with the standard wall functions in application to complex turbulent flows (ref. 7 and 25). This boundary condition is inconsistent with the near-wall analysis. A wall function for the M-S turbulence model obtained from a near-wall analysis is given in reference 3 if a wall function needs to be used. Also an arbitrary ratio of k_t/k_p was used as an inlet boundary condition in a number of boundary layer calculations (ref. 25). In this case, the calculated shear layer expands rapidly so that the turbulence field can adjust itself to the ill-posed inlet boundary condition, (ref. 3).

COMPUTATIONAL RESULTS

Incompressible Turbulent Flow over a Curved Hill

The turbulent flow over a curved hill considered in this paper can be found in references 5 and 9. The unit Reynolds number based on the free stream velocity (U_∞=20 m/sec) is 1.33×10^6/meter. A series of numerical tests on the dependence of the computational results on the grid size, the location of the far field boundary, and the boundary conditions prescribed at the far field boundaries can be found in reference 5. The numerical results presented in this paper are almost independent of these numerical uncertainties.

The calculated pressure distribution on the wall of the curved hill is compared with the measured data in Figure 1, where the pressure coefficient was obtained by normalizing the wall pressure by the free stream dynamic pressure ($0.5\rho U_\infty^2$). It can be seen from this figure that the numerical method does not yield an unphysical oscillatory solution for the mesh with the grid aspect ratio as large as a few tens of thousand and that the calculated pressure distribution compares favorably with the measured data.

The calculated displacement thickness is compared with the measured data in Figure 2. It can be seen in the figure that the calculated result and the measured data compare favorably with each other. The calculated displacement thickness near the inlet boundary is slightly larger than the measured data. This slight discrepancy is attributed to the inlet boundary condition used. In the experiment, the flow was made turbulent using a trip wire located 0.65C upstream of the forward corner of the curved hill. In the numerical calculation, the inlet boundary condition was obtained from experimental data for a fully developed boundary layer flow over a flat plate (ref. 5). This inlet boundary condition is somewhat different from that of the tripped turbulent flow; however, it is considered to be a reasonable approximation to the tripped turbulent flow since development of the internal layer is less dependent on the external boundary layer flow (ref. 5) Inclusion of the trip wire in numerical calculation of the entire flow field is prohibitive at present due to the limitation imposed by the computational resources. At a slightly downstream location, the calculated results are in excellent agreement with the measured data. This excellent agreement is due to the fact that the development of the internal layer on the curved hill is only slightly influenced by the approaching external boundary layer flow (ref. 5). It is shown in the figure that the flow approaching the curved hill is highly retarded due to the strong adverse pressure gradient existing near the leading edge of the curved hill and thus the displacement thickness is increased significantly in this region. The same flow slightly beyond the leading edge is subjected to far stronger favorable pressure gradient and is accelerated enormously. Thus the displacement thickness decreases abruptly. Farther downstream, the internal layer is formed gradually and thus the displacement thickness grows gradually until the flow is subjected to separation at the rear end of the curved hill. Near the separation point, these integral parameters increase abruptly again. The present numerical results show that the wavy nature of the displacement thickness is inherent to the flow over the curved hill. It is also interesting to note that any turbulence model incorporating a wall function method may not be able to describe the turbulence field over the curved hill adequately because of the wavy nature of the boundary layer thickness. For example, the optimal distance from the wall where a wall function method can be applied is obscured because of the rapidly varying boundary layer thickness.

The calculated wall shearing stress is shown in Figure 3, where the friction coefficient was obtained by normalizing the wall shearing stress by the free stream dynamic pressure. The measured data and the computational result obtained using a curvature correction method (ref. 9) are also shown in this figure for comparison. It can be seen in the figure that the calculated wall shearing stress for the curved hill is slightly smaller than the measured data near the inlet boundary. This discrepancy indicates that the inlet boundary condition obtained from a fully developed turbulent boundary layer flow is not quite a good approximation of the flow made turbulent with a trip wire. In the figure, "S" represents the separation location and "R" represents the reattachment location. The M-S turbulence model successfully predicts the small reversed flow region near the rear end of the curved hill. The wall shearing stress obtained using a curvature correction method is in close agreement with the measured data. This accurate result may be due to the use of a boundary layer flow solver which incorporates the measured pressure distribution on the wall. However, the curvature correction method still fails to predict the reversed flow region at the rear end of the curved hill.

The calculated Reynolds stress profiles at a few downstream locations are shown in Figure 4. It can be seen in the figure that the calculated Reynolds stress profile at s=0.710 meters is slightly more spread out than the measured data. This discrepancy is again attributed to the inlet boundary condition obtained from a fully developed boundary layer flow. At farther downstream locations, the calculated and the measured Reynolds stresses are in fair agreement with the measured data. The shape of the Reynolds stress profile at s=0.710 meters is similar to that of wall-bounded simple shear layer flows and it belongs to the external boundary layer flow. It is can be seen in the figure that the strength of the Reynolds stress of the external boundary layer flow decays gradually and that of the internal layer grows rapidly as the fluid travels in the downstream direction. At farther downstream locations, these two Reynolds stress profiles merge together and form a new profile which is similar to that of a wall-bounded simple shear layer flow.

Compressible Turbulent Flows over a Curved Hill

The measured data for the transonic flow over an axisymmetric curved hill at various free stream Mach numbers can be found in references 1, 10, and 11. The unit Reynolds number based on the free stream condition is 13.2×10^6/m for M_∞=0.875 and 10×10^6/m for all other free stream Mach numbers. Details on the grid independence study, boundary conditions, and initial guess can be found in reference 6.

The calculated iso-Mach lines, reproduced from reference 6, are shown in Figure 5 where the incremental Mach number between the contour lines is constant for each free stream Mach number. It can be seen from this figure that the present numerical method can cleanly resolve the transonic flows from low to high transonic free stream Mach numbers. The size of the supersonic pocket for M_∞=0.925 also compares favorably with that obtained using the MacCormack scheme (ref. 11).

The calculated separation and reattachment locations are compared with the measured data and the other numerical results in Figure 6. It is shown in the figure that the Jones-Launder k-ϵ turbulence model (ref. 11) and a k-ϵ turbulence model supplemented with a streamline curvature correction method (ref. 12) fail to predict the reversed flow region at low free stream Mach numbers. At low free stream Mach numbers, the present results compare more favorably with the measured data than do those obtained by the MacCormack scheme using the King-Johnson (K-J) turbulence model (ref. 11). As the free stream Mach number is increased, the present method

slightly under-predicts the size of the reversed flow region compared with the measured data and the numerical results obtained using the K-J turbulence model. This under-prediction of the reversed flow region is a result of the calculated shocks being located slightly downstream of the measured data.

The Reynolds stress profiles for $M_\infty=0.875$ at a few axial locations are shown in Figure 7. At low free stream Mach numbers for which the shock wave - boundary layer interaction does not exist, the flow separation is caused by the turbulent shear stress developing over the forward part of the curved hill. A successful prediction of such a flow depends on the capability of a turbulence model to correctly describe the turbulence field subjected to the streamline curvature (ref. 5 and 6). As shown in this figure, the present numerical results compare more favorably with the measured Reynolds stress than do the other numerical results at x/c=0.69 and 0.75. It is also shown in the figure that the k-ϵ turbulence model with an improved wall function (ref. 26) significantly over-estimates the Reynolds stress at x/c=0.75. Inside the reversed flow region, x/c=1.0, the present numerical result compares less favorably with the measured data than does the one obtained using the K-J turbulence model. This under-prediction in the magnitude of the Reynolds stress is attributed to the calculated shock and the separation point which are located slightly downstream of the measured data.

CONCLUSIONS AND DISCUSSION

Numerical investigations of incompressible and compressible turbulent flows over curved hills are presented. The turbulence is described by a multiple-time-scale turbulence model supplemented with a "partially low Reynolds number" near-wall turbulence model.

For turbulent flows over a curved hill, the mean flow is subjected to extra strains caused by the streamline curvature. The development of the turbulence field over such a curved surface mostly depends on the extra strains. The capability to predict the reversed flow region in turbulent flows over a curved hill rests on the capability of a turbulence model to properly resolve the turbulence field subjected to the strong streamline curvature. It was shown that the present turbulence model can predict the reversed flow region caused by the streamline curvature for both the incompressible and compressible flows while many other turbulence models incorporating a streamline curvature correction method fail to predict such a reversed flow region. The present numerical results also show that the reversed flow region grows extensively due to the shock wave - turbulent boundary layer interaction at high free stream Mach numbers. These numerical results compare favorably with the measured data and the other numerical results obtained using the King-Johnson turbulence model (ref. 11). These computational results also showed that the multiple-time-scale turbulence model yields significantly more accurate solutions than many other turbulence models for the incompressible flow and the more complex compressible flow which includes the supersonic pocket and the nearly incompressible reversed flow region.

The density-weighted average of the Navier-Stokes equations yields the same turbulent flow equations for incompressible and compressible flows. This suggests that the same turbulence equations can be used for incompressible and compressible flows. However, the use of turbulence models developed for incompressible turbulent flows in numerical calculations of compressible turbulent flows yields poor numerical results, and vice versa. Thus a number of compressibility correction methods were proposed and are in use for compressible flows. On the other hand, it

was shown in this paper that the multiple-time-scale turbulence model yields equally accurate numerical results for both incompressible and compressible flows without the use of a compressibility correction. In this regard, the closure level of the multiple-time-scale turbulence model is more consistent with the underlying mathematical assumption of the density-weighted average than that of other turbulence models which include one or another compressibility correction.

REFERENCES

1. S. J. Kline, B. J. Cantwell & G. M. Lilley (ed) Proc 1980-1981 AFOSR-HTTM Stanford Conference on Complex Turbulent Flows, vol. 1-3, Thermoscience Div., Stanford University, 1982.
2. Persen, L. N. "Concepts of Turbulence and CFD Applications", Progress in Aerospace Sciences, 23, 167-???, 1986.
3. S.-W. Kim and C.-P. Chen, "A Multiple-Time-Scale Turbulence model Based on Variable Partitioning of the Turbulent Kinetic Energy Spectrum", Numer. Heat Transfer, Part B, vol. 16, pp. 193-211, 1989. Also available as NASA CR-179222, 1988.
4. S.-W. Kim, "Calculation of Reattaching Shear Layers in Divergent Channel with a Multiple-Time-Scale Turbulence Model," AIAA Paper 90-0047, 1990.
5. S.-W. Kim, "Numerical Investigation of an Internal Layer in Turbulent Flow over a Curved Hill," NASA TM-102230, 1989.
6. S.-W. Kim, "Numerical Investigation of Separated Transonic Turbulent Flows with a Multiple-Time-Scale Turbulence Model," To appear in Numerical Heat Transfer, 1990, Also available as NASA TM-102499, 1990.
7. K. Hanjelic, B. E. Launder, and R. Schiestel, "Multiple-Time-Scale Concepts in Turbulent Shear Flows" in L. J. S. Bradbury, F. Durst, B. E. Launder, F. W. Schmidt, and J. H. Whitelaw, (eds.), Turbulent Shear Flows, vol. 2, pp. 36-49, Springer-Verlag, New York, 1980.
8. Bradshaw, P. "Effects of Streamline Curvature on Turbulent Flow," AGARDograph 169, 1973.
9. V. Baskaran, A. J. Smits and P. N. Joubert, "A Turbulent Flow over a Curved Hill: Part I. Growth of an Internal Boundary Layer, J. Fluid Mechanics, vol. 182, pp. 47-83, 1987.
10. W. D. Bachalo and D. A. Johnson, "An Investigation of Transonic Turbulent Boundary Layer Separation Generated on an Axisymmetric Flow Model," AIAA Paper 79-1479, 1979.
11. D. A. Johnson, "Transonic Separated Flow Prediction with an Eddy-Viscosity/Reynolds-Stress Closure Model," J. AIAA, vol. 25, pp. 252-259, 1987.
12. C. C. Horstman and D. A. Johnson, "Prediction of Transonic Separated Flows," J. AIAA, vol. 22, No. 7, pp. 1001-1003, 1984.
13. D. A. Johnson, C. C. Horstman and W. D. Bachalo, "Comparison Between Experiment and Prediction for a Transonic Turbulent Separated Flow," J. AIAA, vol. 20, pp. 737-744, 1982.
14. F. M. White, Viscous Fluid Flow, McGraw-Hill, New York, 1974.
15. M. J. Zucrow and J. D. Hoffman, Gas Dynamics, vol. 1, John Wiley & Sons, New York, 1976.
16. S.-W. Kim, "A Control-Volume Based Reynolds Averaged Navier-Stokes Equation Solver Valid at All Flow Velocities," NASA TM-101488, 1989.
17. R. M. Beam and R. F. Warming, "An Implicit Factored Scheme for the Compressible Navier-Stokes Equations," J. AIAA, vol. 16, pp. 393-402, 1978.
18. R. W. MacCormack, "A Numerical Method for Solving the Equations of Compressible Viscous Flow," J. AIAA, vol. 20, pp. 1275-1281, 1982.

19. J. L. Steiger and R. F. Warming, "Flux-Splitting of the Invicid Gasdynamic Equations with Application to Finite Difference Method," <u>J. Comput. Physics</u>, vol. 40, pp. 263-293, 1981.

20. S. E. Rogers, D. Kwak, and J. L. C. Chang, "INS3D - An Incompressible Navier-Stokes Code in Generalized Three-Dimensional Coordinates," NASA TM-100012, 1987.

21. Tennekes, H. & Lumley, J. L. <u>A First Course in Turbulence</u>, MIT Press, London, 1972.

22. S.-W. Kim, "A Near-Wall Turbulence Model and Its Application to Fully Developed Turbulent Channel and Pipe Flows," <u>Numer. Heat Transfer</u>, Part B, vol. 17, pp. 101-122, 1990. Also available as NASA TM-101399, 1988.

23. V. G. Harris, J. A. H. Graham, and S. Corrsin, "Further Experiments in Nearly Homogeneous Turbulent Shear Flow," <u>J. Fluid Mech.</u>, vol. 81, pp. 657-687, 1977.

24. F. H. Harlow and P. I. Nakayama, "Transport of Turbulence Energy Decay Rate," Los Alamos Sci. Lab., LA-3854, 1968.

25. G. Fabris, P. T. Harsha, and R. B. Edelman, "Multiple-Scale Turbulence Modelling of Boundary Layer Flows for Scramjet Applications," NASA CR-3433, 1981.

26. M. W. Rubesin and J. R. Viegas, "Turbulence Modelling in Transonic Flow," Transonic Symposium - Theory, Application and Experiment, NASA Langley Research Center, Hampton, Virginia, April, 1988.
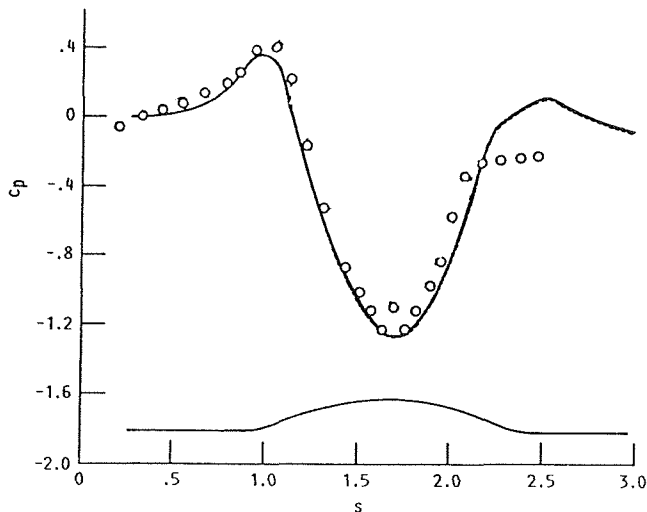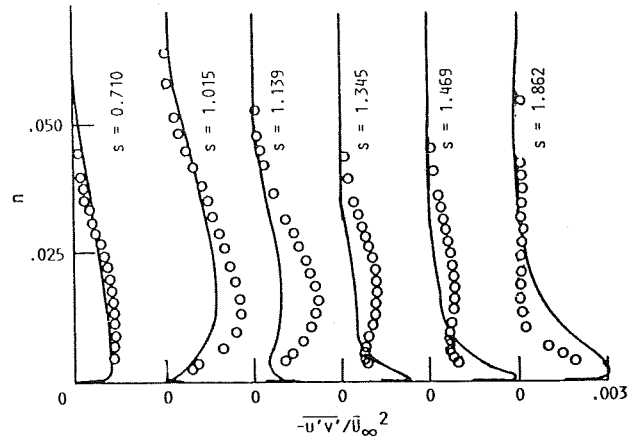
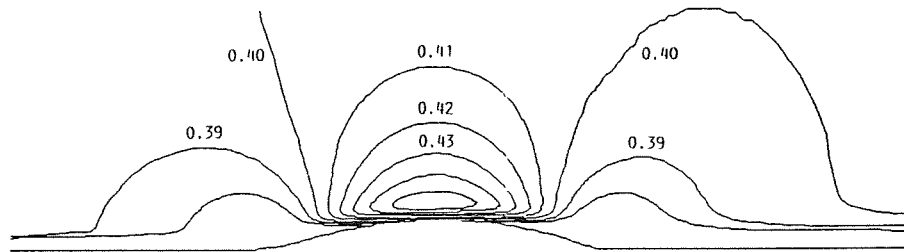1. Pressure distribution, O: measured data, ———: numerical result.
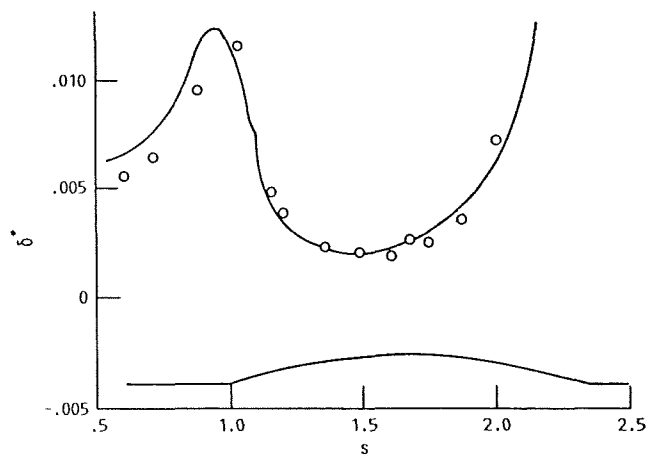
2. Displacement thickness, O: measured data, ———: numerical result.
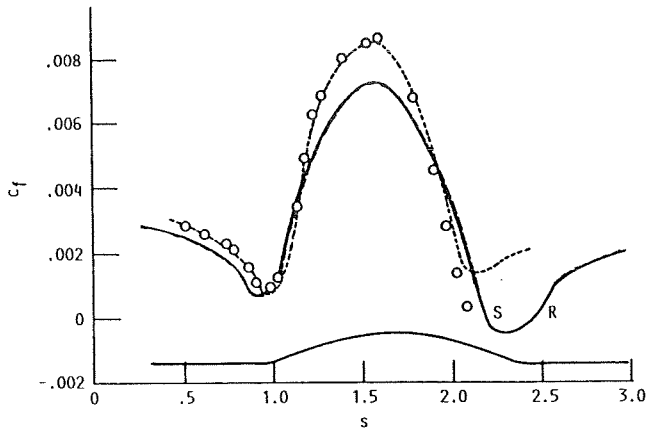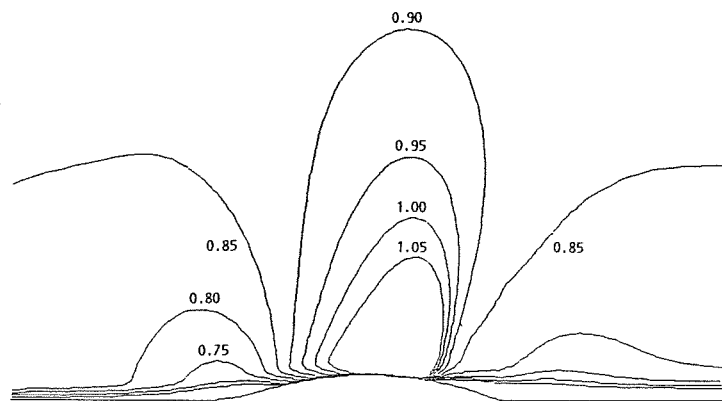
3. Wall shearing stress, O: measured data, ———: present numerical result, -----: numerical result (ref. 9).

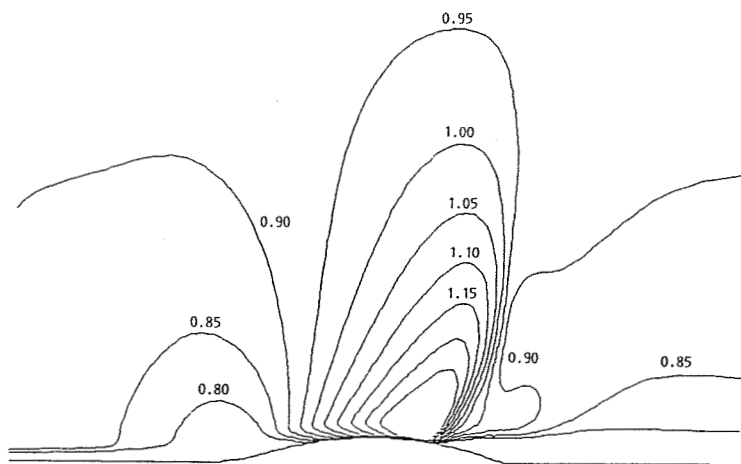4. Reynolds stress profiles, O: measured data, ———: numerical result.
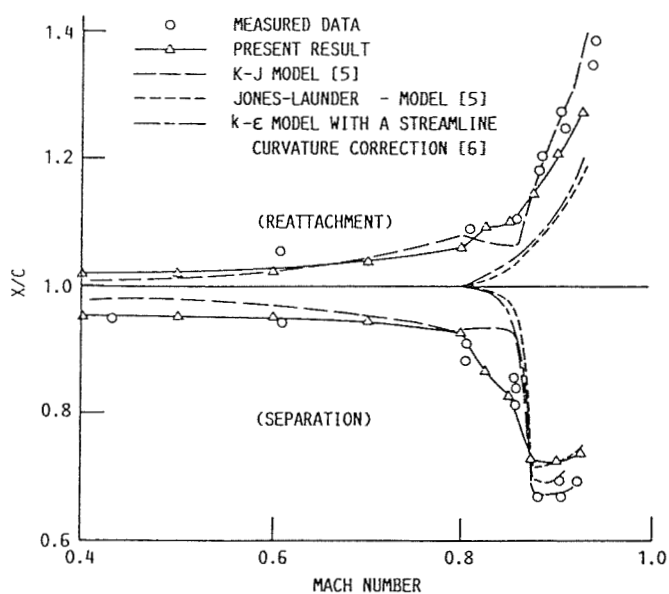

(a) $M_\infty = 0.40$,
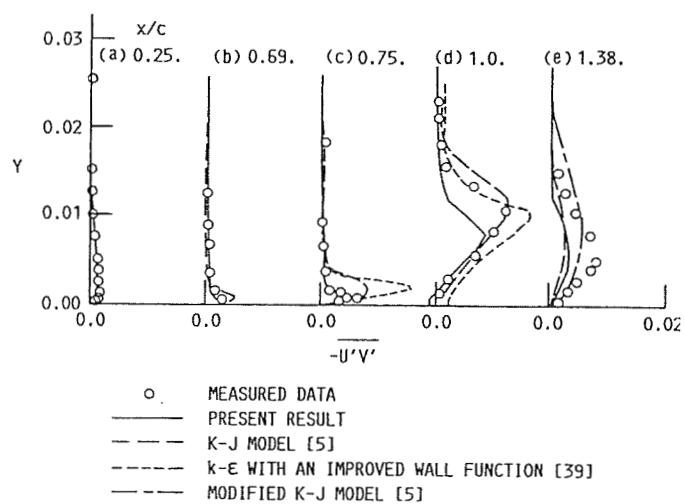

(b) $M_\infty = 0.875$,

5. Iso-Mach lines.

406

(c) $M_\infty = 0.925$.

5. Concluded.

6. Flow separation and reattachment locations

7. Reynolds stress profiles